

Three-dimensional optoacoustic tomography at video rate

A. Buehler, X. L. Deán-Ben, J. Claussen, V. Ntziachristos and D. Razansky*

Institute for Biological and Medical Imaging, Technische Universität München and Helmholtz Zentrum München, Ingolstädter Landstraße 1, D-85764 Neuherberg, Germany
*dr@tum.de

Abstract: Using optoacoustic excitation, a complete volumetric tomographic data sets from the imaged object can in principle be generated with a single interrogating laser pulse. Thus, optoacoustic imaging intrinsically has the potential for fast three-dimensional imaging. We have developed a system capable of acquiring volumetric optoacoustic data in real time and showcase in this work the undocumented capacity to generate high resolution three-dimensional optoacoustic images at a rate of 10Hz, currently mainly limited by the pulse repetition rate of the excitation laser.

©2012 Optical Society of America

OCIS codes: (170.3880) Medical and biological imaging; (110.5120) Photoacoustic imaging; (110.6955) Tomographic imaging.

References and links

1. L. V. Wang, "Multiscale photoacoustic microscopy and computed tomography," *Nat. Photonics* **3**(9), 503–509 (2009).
2. M. H. Xu and L. H. V. Wang, "Photoacoustic imaging in biomedicine," *Rev. Sci. Instrum.* **77**(4), 041101 (2006).
3. V. Ntziachristos, "Going deeper than microscopy: the optical imaging frontier in biology," *Nat. Methods* **7**(8), 603–614 (2010).
4. V. Ntziachristos and D. Razansky, "Molecular imaging by means of multispectral optoacoustic tomography (MSOT)," *Chem. Rev.* **110**(5), 2783–2794 (2010).
5. L. V. Wang, "Prospects of photoacoustic tomography," *Med. Phys.* **35**(12), 5758–5767 (2008).
6. L. V. Wang, "Tutorial on photoacoustic microscopy and computed tomography," *IEEE J. Sel. Top. Quantum Electron.* **14**(1), 171–179 (2008).
7. D. Razansky, A. Buehler, and V. Ntziachristos, "Volumetric real-time multispectral optoacoustic tomography of biomarkers," *Nat. Protoc.* **6**(8), 1121–1129 (2011).
8. R. Ma, A. Taruttis, V. Ntziachristos, and D. Razansky, "Multispectral optoacoustic tomography (MSOT) scanner for whole-body small animal imaging," *Opt. Express* **17**(24), 21414–21426 (2009).
9. D. Razansky, M. Distel, C. Vinegoni, R. Ma, N. Perrimon, R. W. Koster, and V. Ntziachristos, "Multispectral opto-acoustic tomography of deep-seated fluorescent proteins in vivo," *Nat. Photonics* **3**(7), 412–417 (2009).
10. D. Razansky, C. Vinegoni, and V. Ntziachristos, "Multispectral photoacoustic imaging of fluorochromes in small animals," *Opt. Lett.* **32**(19), 2891–2893 (2007).
11. D. Razansky, C. Vinegoni, and V. Ntziachristos, "Imaging of mesoscopic-scale organisms using selective-plane optoacoustic tomography," *Phys. Med. Biol.* **54**(9), 2769–2777 (2009).
12. J. Gamelin, A. Maurudis, A. Aguirre, F. Huang, P. Y. Guo, L. V. Wang, and Q. Zhu, "A real-time photoacoustic tomography system for small animals," *Opt. Express* **17**(13), 10489–10498 (2009).
13. S. A. Ermilov, T. Khamapirad, A. Conjusteau, M. H. Leonard, R. Lacewell, K. Mehta, T. Miller, and A. A. Oraevsky, "Laser optoacoustic imaging system for detection of breast cancer," *J. Biomed. Opt.* **14**(2), 024007 (2009).
14. B. Z. Yin, D. Xing, Y. Wang, Y. G. Zeng, Y. Tan, and Q. Chen, "Fast photoacoustic imaging system based on 320-element linear transducer array," *Phys. Med. Biol.* **49**(7), 1339–1346 (2004).
15. A. Buehler, E. Herzog, D. Razansky, and V. Ntziachristos, "Video rate optoacoustic tomography of mouse kidney perfusion," *Opt. Lett.* **35**(14), 2475–2477 (2010).
16. R. A. Kruger, R. B. Lam, D. R. Reinecke, S. P. Del Rio, and R. P. Doyle, "Photoacoustic angiography of the breast," *Med. Phys.* **37**(11), 6096–6100 (2010).
17. H. P. Brecht, R. Su, M. Fronheiser, S. A. Ermilov, A. Conjusteau, and A. A. Oraevsky, "Whole-body three-dimensional optoacoustic tomography system for small animals," *J. Biomed. Opt.* **14**(6), 064007 (2009).
18. P. Ephrat, M. Roumeliotis, F. S. Prato, and J. J. L. Carson, "Four-dimensional photoacoustic imaging of moving targets," *Opt. Express* **16**(26), 21570–21581 (2008).
19. X. L. Deán-Ben, R. Ma, D. Razansky, and V. Ntziachristos, "Statistical approach for optoacoustic image reconstruction in the presence of strong acoustic heterogeneities," *IEEE Trans. Med. Imaging* **30**(2), 401–408 (2011).

20. J. A. Jensen, "Field: A program for simulating ultrasound systems," *Med. Biol. Eng. Comput.* **34**, 351–353 (1996).
 21. J. A. Jensen and N. B. Svendsen, "Calculation of pressure fields from arbitrarily shaped, apodized, and excited ultrasound transducers," *IEEE Trans. Ultrason. Ferroelectr. Freq. Control* **39**(2), 262–267 (1992).
 22. M. Xu and L. V. Wang, "Analytic explanation of spatial resolution related to bandwidth and detector aperture size in thermoacoustic or photoacoustic reconstruction," *Phys. Rev. E Stat. Nonlin. Soft Matter Phys.* **67**(5), 056605 (2003).
 23. S. C. Grubb, G. A. Churchill, and M. A. Bogue, "A collaborative database of inbred mouse strain characteristics," *Bioinformatics* **20**(16), 2857–2859 (2004).
-

1. Introduction

Optoacoustic imaging attains high resolution maps of optical absorption by measuring ultrasonic responses generated by thermoelastic expansion of tissue structures following the deposition of short light pulses in the imaged object [1]. Essentially, it provides the ability to perform optical imaging at high resolution deep inside highly scattering tissues. A multitude of new pre-clinical and clinical directions have been so far explored using optoacoustics, ranging from anatomical visualization to functional and molecular imaging [1–7].

Tomographic optoacoustic implementations typically employ signal detection along multiple directions (projections). To simplify the hardware requirements and reduce cost, optoacoustic tomography can be reduced to two dimensions by selectively acquiring signals generated within a certain plane using focused ultrasonic elements [8–12]. To speed up signal acquisition, systems have been implemented which use arrays from clinical ultrasound imaging systems or custom linear arrays [13, 14]. We have recently reported on the development of a cross-sectional real-time imaging scanner for small animal applications, which utilized cylindrically-focused circular transducer array covering a solid angle of 172° around the imaged object [15]. Three-dimensional optoacoustic tomography has been also implemented using spiral distribution of 128 transducers over a hemi-spherical bowl [16] or using a 64 element unfocused transducer array rotated around the sample [17], however, no real time imaging capacity was possible with this implementation. Recently, real time three-dimensional tomography was showcased by using a sparse distribution of a small number of transducers to image simple three dimensional structures consisting of rods or point-sources, albeit with poor resolution as only 15 detectors were used [18].

Efficient implementation of three-dimensional data collection is overall challenging as it requires simultaneous collection of time-resolved optoacoustic signals from a large number of points (projections) around the imaged object. Nevertheless, there are potentially advantages in offering three dimensional real time imaging. First, dynamic processes, such as the biodistribution of molecular probes, can be monitored in the entire volume of interest. Second, motion artifacts that could degrade the image quality when imaging living specimen can be avoided. Finally, real-time performance can obviously accelerate the time required for experiments or clinical measurements.

Herein we implemented a real-time three dimensional optoacoustic imaging system suitable for small animal dimensions. The system utilizes simultaneous acquisition of signals from 256 points distributed over a spherical surface surrounding the sample. Thereby, volumetric reconstructions can be obtained at 10 frames per second (pulse repetition rate of the laser). In the following, we present a description of the imaging system and show its capability to image complex static structures and dynamic processes in real time.

2. Materials and methods

2.1 Imaging system

A layout of the imaging system is depicted in Fig. 1(a). It is based on a custom-made 256 element transducer array (Imasonic SaS, Voray, France) covering a solid angle of 240° in azimuth and 75° in elevation around the imaged object. In between the two hemispheres there is a 1.9cm gap left for illumination purposes. The individual elements are manufactured using piezocomposite technology with a central frequency of approximately 3.3 MHz and bandwidth (FWHM) of 4.3MHz (Fig. 1 (b)). The individual elements, having dimensions of 4

$\times 4 \text{ mm}^2$, are arranged in space as depicted in Fig. 1(c). Sections along the xy -, xz - and yz -plane of the simulated point target sensitivity field of a single transducer are shown in the first column of Fig. 1(d) while sections through the combined sensitivity field, i.e. summation of the sensitivity fields of all the elements, are displayed in the second column of Fig. 1(d). In this way, an imaging region of about $10 \times 10 \times 10 \text{ mm}^3$ can be covered using a single laser pulse (this corresponds to a region within -6dB of the combined sensitivity field). Excitation light originates from a tuneable (680–900 nm) optical parametric oscillator laser (Phocus, Oportek Inc., Carlsbad, CA), delivering $<10\text{ns}$ duration pulses with repetition frequency of 10 Hz. The beam is guided into a custom-made silica fused-end fiber bundle (CeramOptics GmbH, Bonn, Germany) consisting of 630 fibers partitioned into 10 arms. The individual arms are attached at the illumination gap to create a ring-shaped illumination pattern of approximately 9mm width upon the surface of the imaged object. The optoacoustic signals are digitized at 40 megasamples per second frequency by custom-made multi-channel analog to digital converter. The laser's Q-switch provides the trigger for the acquisition. The sample is placed in a specially designed sample holder comprising a transparent and water-impermeable membrane that averts direct contact of the object with water. A linear stage (LTM 80F 300, OWIS GmbH, Staufen, Germany) allows linear translation of the sample holder in the axial z direction for acquisition of three-dimensional data sets from different regions of the sample.

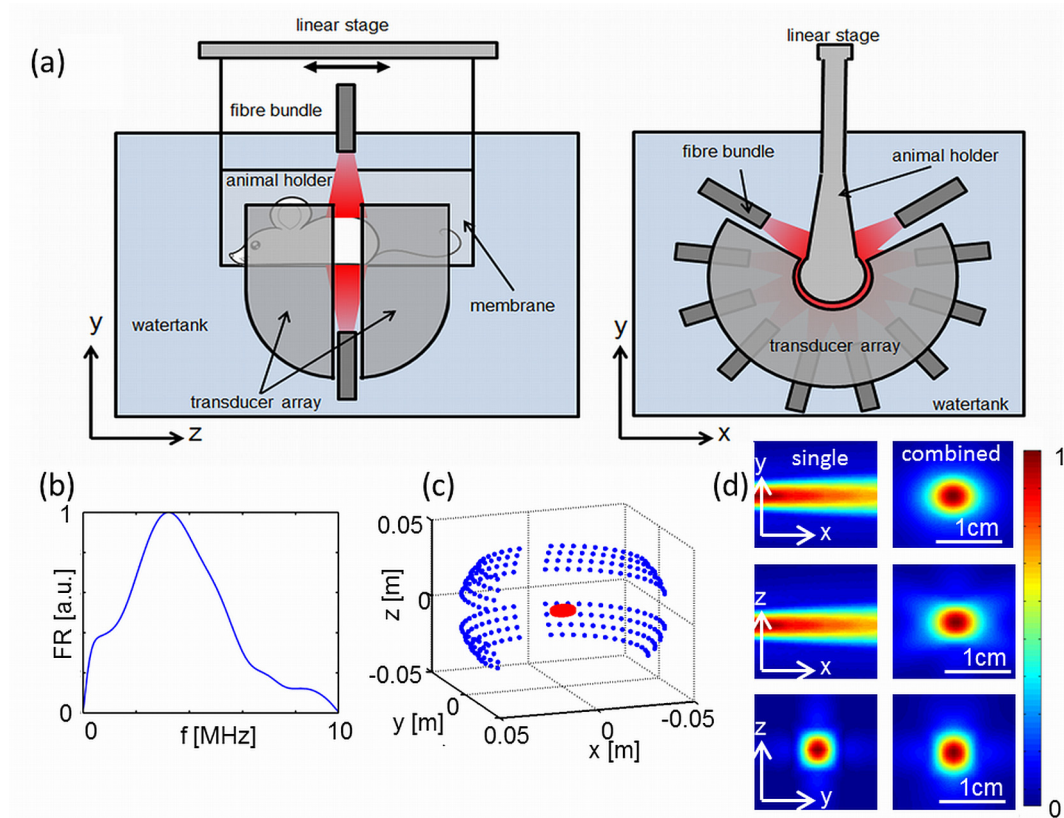


Fig. 1. The imaging system. (a) A schematic representation of the major components seen from two different directions. (b) Frequency response of the transducer. (c) Arrangement in space of the individual transducer elements. (d) Sections through the sensitivity field of a single transducer element (first column) and the combined sensitivity field of the system (second column). The sections are centered at (0,0,0). The single transducer element is located at $(-5,0,0)$ cm. The -6dB combined sensitivity field region is depicted in red in (b).

2.2 Signal processing and image reconstruction

In a first step, the signals are bandpassfiltered with a Chebychev filter with cut-off frequencies of 100 kHz and 7 MHz to remove low and high frequency noise. The filtered signals are subsequently used for image reconstruction with a modified back-projection algorithm [19]. Specifically, a discretized version of the back-projection formula, which ignores solid angle weighting, is used. Instead, the signals are weighted with the point target sensitivity field of the particular transducer element so that the absorbed laser energy $H(r'_j)$ at a point r'_j is given by

$$H(r'_j) = \sum_i S_i(r'_j) \left[p(r_i, t_{ij}) - t_{ij} \frac{\partial p(r_i, t_{ij})}{\partial t} \right] \quad (1)$$

where $S_i(r'_j)$ is the sensitivity of the i -th element at for a signal generated at r'_j and $p(r_i, t_{ij})$ is the pressure measured at the position of the i -th element r_i at instant $t_{ij} = |r'_j - r_i| c^{-1}$. This kind of weighting can reduce streak-type artifacts typically present in back-projection reconstructions in areas outside the object where the sensitivity of the elements is generally low. The sensitivity field of a single transducer element (Fig. 1(d) first column) was computed numerically using an open-source Field II software [20, 21]. In order to image larger objects, data sets at various positions along the z -axis can be acquired by translating the animal holder. In this way, the initial 1 cm³ volume is first reconstructed for each data set, while the merge of all the initial reconstructions into a larger volume is done off-line by averaging the intersecting parts.

2.3 System characterization

Basic imaging performance was tested with two different phantoms using 760 nm illumination. All images were acquired without averaging, i.e. using single laser pulses. The first phantom consisted of a light scattering cylinder with a diameter of 1.9 cm containing a 100 μ m in diameter black absorbing microsphere (Cospheric LLC Santa Barbara, CA). The light scattering phantom is obtained by adding 1.2% by volume of Intralipid (Sigma-Aldrich, St. Louis, MO) into an agar solution (1.3% by weight). The microsphere was moved in the imaging plane to three different positions, namely (0,0,0), (-5,0,0) and (-10,0,0) mm, in order to characterize the resolution of the system in different directions. For each position, the corresponding point-spread-function was calculated with the back-projection algorithm within a volume of 22 x 24 x 3mm³ consisting of 600 x 600 x 75 voxels. The second phantom was used in order to showcase the real-time performance of the system. It consisted of a transparent tube with an inner diameter of 300 μ m embedded in a scattering agar cylinder. The tube was perfused with diluted ink yielding an absorption coefficient of 5cm⁻¹. The ROI was 21 x 21 x 10mm³ while the reconstruction was done using 201 x 201 x 100 voxels.

2.4 Mouse imaging

To test performance in the presence of realistic heterogeneous tissues, we have imaged an excised mouse heart, which was again embedded into a scattering agar cylinder. Likewise, the reconstruction was done with the sensitivity-weighted back-projection algorithm. The ROI contained a volume of 15 x 15 x 10 mm³ and consisted of 151 x 151 x 100 voxels.

Whole body imaging performance was showcased with a 10 days old CD1 mouse. The mouse was euthanized according to approved institutional regulations regarding animal experiments while the hair was removed with shaving cream. It was placed in the animal holder in supine position and scanned with a 200 μ m steps along its longitudinal axis over a total distance of 4cm. The imaging wavelength was 760nm. For each scanning position, a volume of 16x16x8mm³ was reconstructed using 161x161x81 voxels. As previously described, the individual volumes were merged by averaging the intersecting parts.

Finally, several *in vivo* experiments were performed in order to assess the real-time operation. In the first experiment, heartbeat of a baby mouse was visualized. For this, a 10 days old CD1 mouse was anesthetized, shaved and placed in prone position into the animal holder. The water temperature was stabilized at 32°C. Ultrasound gel was used to improve acoustic coupling. Signals were acquired at the heart level with a frame rate of 10 Hz. The laser wavelength was set to 850nm. In the second experiment, perfusion of contrast agent through the brain of an adult atymic CD1 mouse was visualized. The mouse was injected with 130nmoles of Indocyaninegreen (ICG) through its tail vein while imaging was done at 800nm wavelength (near the absorption peak of ICG) with a frame rate of 10Hz.

3. Results

3.1 System characterization

Figure 2(a)-2(f) depicts cross-sectional images of the microparticle with the first and second row representing cross-sections within the xy-plane and yz-plane, respectively. The positions of the microsphere are (0,0,0) mm (first column), (-5,0,0) mm (second column) and (-10,0,0) mm (third column). Clearly, the resolution is anisotropic and is also not constant along some of the axis. The radial and transverse resolutions are subsequently estimated as the full width at half maximum (FWHM) along the radial and transverse directions. The radial resolution of approximately 200 μ m is only bandwidth limited and is thus spatially invariant, in good agreement with the theoretically predicted value [2, 22]. The transverse resolution however varies significantly between ~200 μ m in the center of the array, degrading to approximately 850 μ m at a distance of 10mm from the center, as shown in Fig. 2. The reconstructed microsphere at the center of the transducer array is slightly elongated towards the z-direction. The reason for this is the reduced elevational aperture (75°) of the system, which provides relatively limited view in this direction. A larger elevational angle and more transducer elements could therefore improve the resolution. The 3D realtime imaging capability has been showcased by monitoring ink flow through a plastic tube. A video of the ink flowing through the tubing imaged at 10 frames/s is available on line ([Media 1](#)).

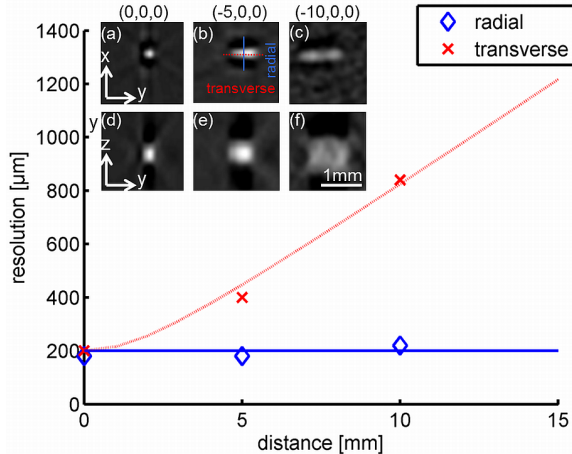


Fig. 2. Radial and transversal resolution of the system as a function of the position. The insets show reconstructed images of a 100 μ m microsphere located at the coordinates (0,0,0) mm (first column), (-5,0,0) mm (second column), and (-10,0,0) mm (third column). The first row depicts the cross-sections through the microsphere along the xy-plane. The second row the cross-sections along the yz-plane.

3.2 Mouse data

Figure 3 depicts the MIP images of the excised mouse heart along two representative directions along with a cross-sectional slice and a photograph of the excised mouse heart.

Single shot images are shown (no averaging). A rotational movie showing the MIP from different viewing angles is available in the online version of the journal ([Media 2](#)). High resolution anatomy of the heart can be clearly identified in the images, including the two ventricles separated by the septum, the aortic arch as well as some other coronary vessels.

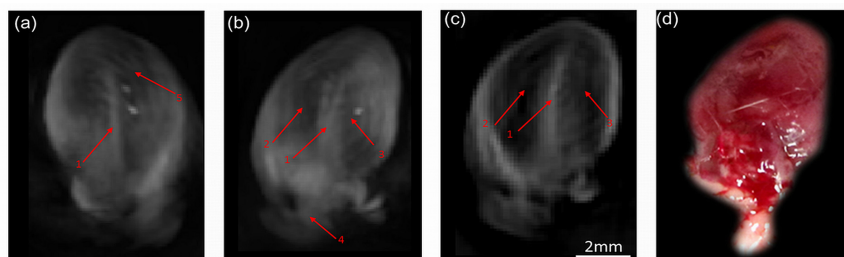


Fig. 3. Single shot imaging of an excised mouse heart. The maximum intensity projection (MIP) of the heart along two directions is shown in (a) and (b). (c) depicts a cross-sectional slice through the heart. (d) shows a photograph of the mouse heart. A movie file ([Media 2](#)) showing the volume rotating is available in the online version of the journal. 1. septum, 2. right ventricle, 3. left ventricle, 4. aorta, 5. coronary vessels

Figure 4(a) depicts MIP optoacoustic image of the sacrificed babymouse with the corresponding photograph shown in Fig. 4(b). The rotational video is further available on line ([Media 3](#)). Since optoacoustic imaging is dominantly sensitive to hemoglobin-based contrast, mainly the vasculature of the animal is visible. High resolution details (sagittal sinus, the frontal cerebral arteries or the longitudinal fissure of cerebrum) are also visible when zooming into the mouse brain (Fig. 4, panels (c)-(f)).

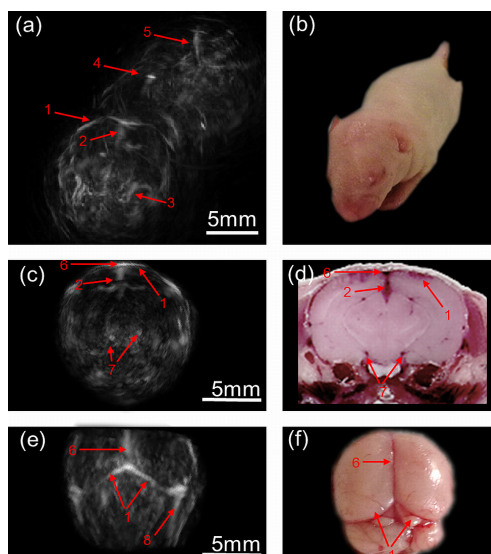


Fig. 4. Volumetric reconstruction of a babymouse. (a) depicts the MIP of the mouse vasculature. A movie file ([Media 3](#)) of the reconstruction from different angles is available online. (b) A photograph of the babymouse to indicate the orientation of the volumetric reconstruction. (c) depicts the MIP of a 1cm thick region through the mouse brain, (d) a corresponding cryoslice, (e) the MIP from the top, (f) a photograph of an excised mouse brain. 1. transverse sinus, 2. longitudinal fissure of cerebrum, 3. left supraorbital vein, 4. thoracic aorta, 5. right iliac artery, 6. sagittal sinus, 7. frontal cerebral arteries, 8. superior cerebral vein.

Figure 5 shows cross-sectional reconstructions of the 10 days old mouse in the heart region during a diastolic (a) and systolic (b) phase of the heart cycle as well as a photograph of a cryoslice through a mouse's heart area for comparison. An online video ([Media 4](#)) is also available. The video is displayed in slow motion at 5 frames/s, even though the images have

been acquired at 10 frames/s. One can recognize the heart, including the septum (1), the two ventricles (2 and 3) and the lung (4). Both in the images and the video, one can clearly see the change of the size of the heart due to the pumping movement. An increase of the signal intensity in the left ventricle during the diastolic phase is also visible due to the filling of the ventricle with oxygen enriched blood coming from the lung. In the movie file it is also possible to distinguish between the heart and breathing motions. The breathing motions are less frequent and have larger magnitude as compared to the heart movements. Naturally, the reconstructions from the heart area have generally poor quality and low resolution, presumably due to propagation artifacts introduced by lungs which contain acoustically-mismatched air cavities. In addition, the heart rate of mice may vary between 282 ± 57 beats per minute for newborn mice to 632 ± 51 beats per minute for adult ones [23]. Consequently, the imaging rate of 10 Hz is barely sufficient to capture different states of the heart cycle.

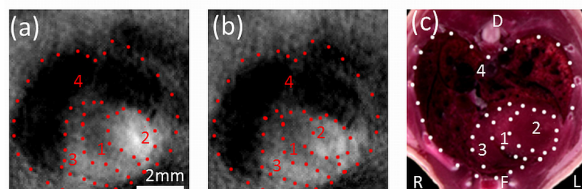


Fig. 5. Cross-sectional reconstructions of a babymouse at the heart region during a diastolic (a) and systolic (b) phase. 1. septum, 2. left ventricle, 3. right ventricle, 4. lung. (c) depicts a cryoslice through the heart area of a mouse for comparison. A movie file ([Media 4](#)) showing the heart movements is available on line.

Finally, Fig. 6 depicts perfusion of ICG through the brain of an adult mouse. Panels (a)-(c) correspond to MIP images along the z-axis at three different time points while (d)-(f) are MIPs along the y-direction captured at the same time points. One can clearly recognize an enhancement in the vasculature contrast following injection of the ICG. Panel (g) depicts the average optoacoustic signal strength in the vein indicated by the white arrow. Although the data is affected by laser energy fluctuations, a clear tendency is visible. During the first 10 seconds the signal is constant while a sudden increase of the signal strength occurs right afterward due to the ICG injection, followed by a plateau in the optoacoustic signal strength.

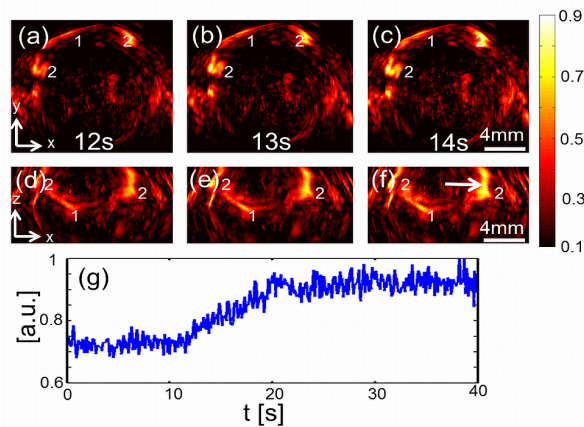


Fig. 6. 3D imaging of brain perfusion after injection of ICG. (a) - (c) MIP of the reconstructed volume along the z-direction at three different time points. (d) - (f) corresponding MIP along the y-axis. (g) signal intensity as a function of time in the vessel indicated by the arrow in (f). 1, transverse sinus, 2, superior cerebellar vein. A video ([Media 5](#)) is available on line.

4. Discussion and conclusions

The optoacoustic phenomenon is unique in a way it allows to generate complete volumetric tomographic data set from the imaged object using a single interrogating laser pulse. This possibility does not exist in other imaging modalities as it is usually necessary to perform sequential excitation of the object from multiple source locations in order to acquire tomographic data required for efficient volumetric image reconstructions. Yet, multiple technical limitations, related to lack of appropriate ultrasound detection technology, digital sampling and processing capacities, hindered so far effective implementation of real-time 3D optoacoustic imaging and tomography.

Herein we developed an optoacoustic tomography system for three-dimensional real-time imaging, which presents important advantages over previously developed scanning systems used for volumetric optoacoustic reconstructions. It was shown possible to attain volumetric optoacoustic reconstructions with a single laser pulse using simultaneous acquisition of optoacoustic responses from 256 locations (projections around the object). The resulting images were therefore significantly less affected by animal motion, which has improved spatial resolution and overall imaging accuracy. We have also shown that a sequence of three-dimensional images at a frame rate of 10 Hz can be retrieved with the system, which allows tracing dynamic events such as perfusion of contrast agents, breathing and heartbeat. In the current implementation, cross-sectional (2D) images are obtained in real-time, while we are currently working on achieving fast 3D reconstructions using graphical processing unit (GPU). The imaging performance of the system was verified in both phantom and in-vivo experiments.

In this work, due to the relatively high concentration of the ICG probe, it was possible to track its biodistribution in real time by single-wavelength imaging at its peak absorption wavelength. However, for significantly lower concentrations of the probe, it might be necessary to perform imaging at multiple wavelengths and spectral unmixing in order to effectively determine probe location in the presence of absorbing background. In the current system implementation, the resolution is anisotropic and also degrades away from the center of the transducer array. This space dependent resolution is a combined effect of the number of transducer elements and their size. Nevertheless, degradation of the spatial resolution due to the final detector size may be improved upon using model-based reconstruction approaches, which allow taking into consideration shape and size of the detection elements and may also reduce the streak artifacts typical for reconstructions made with the backprojection algorithms. Overall, an optimized element distribution or higher number of elements may help to improve the spatial resolution performance.

Acknowledgments

The research leading to these results has received funding from the European Union [European Research Council, *ERC-2009-AdG-233161* and *ERC-2010-StG-260991*].